

# Gravitational waves from vacuum first-order phase transitions: from the envelope to the lattice

Daniel Cutting,<sup>1,2,\*</sup> Mark Hindmarsh,<sup>2,†</sup> and David J. Weir<sup>2,‡</sup>

<sup>1</sup>*Department of Physics and Astronomy, University of Sussex, Falmer, Brighton BN1 9QH, U.K.*

<sup>2</sup>*Department of Physics and Helsinki Institute of Physics, PL 64, FI-00014 University of Helsinki, Finland*

(Dated: June 15, 2018)

We conduct large scale numerical simulations of gravitational wave production at a first-order vacuum phase transition. We find a power law for the gravitational wave power spectrum at high wavenumber which falls off as  $k^{-1.5}$  rather than the  $k^{-1}$  produced by the envelope approximation. The peak of the power spectrum is shifted to slightly lower wave numbers from that of the envelope approximation. The envelope approximation reproduces our results for the peak power less well, agreeing only to within an order of magnitude. After the bubbles finish colliding the scalar field oscillates around the true vacuum. An additional feature is produced in the UV of the gravitational wave power spectrum, and this continues to grow linearly until the end of our simulation. The additional feature peaks at a length scale close to the bubble wall thickness and is shown to have a negligible contribution to the energy in gravitational waves, providing the scalar field mass is much smaller than the Planck mass.

## I. INTRODUCTION

The first direct detection of gravitational waves [1, 2] has brought in a new era of gravitational wave astronomy. Future space based gravitational wave observatories such as LISA [3] hold great promise for cosmology [4]. LISA's planned sensitivity band peaks at lower frequencies than ground based detectors. It therefore will have much greater sensitivity to gravitational waves originating from process in the very early universe. Cosmological first-order phase transitions are one such process, and LISA's sensitivity window allows it to probe electroweak phase transitions in many extensions of the Standard Model [5, 6].

In a cosmological first-order phase transition, the universe changes from a metastable high energy (symmetric) phase to a stable lower energy (broken) phase. This occurs through the quantum or thermal nucleation of bubbles of the broken phase [7–9], separated from the surrounding unbroken phase by a thin wall. These bubbles then expand, collide and eventually coalesce. This process generates shear stresses which in turn source gravitational waves [10, 11].

Early work focussed on characterising the signal from a phase transition that occurs in vacuum [12]. In such a transition, the bubble wall quickly accelerates to ultra-relativistic velocities.

A model of such a scenario was developed, termed the envelope approximation [13]. In this model, the shear stresses are assumed to be concentrated in an infinitesimally thin shell located at the bubble wall. Upon the collision of the bubble walls, the shear stress is assumed to dissipate, and so any regions where bubbles overlap

are ignored. The characteristic gravitational wave power spectrum from the envelope approximation is a broken power law in wave number  $k$ , where the spectrum rises as  $k^3$  from the low-wavenumber (IR) direction and falls off as  $k^{-1}$  in the high-wavenumber (UV) direction. The peak of the broken power law is associated with the length scale of the average bubble separation  $R_*$ .

Although the envelope approximation was originally created for bubbles expanding in vacuum it was quickly applied to thermal first-order phase transitions, in which the scalar bubbles expand in a hot plasma [14–16]. In this case frictional effects from the plasma typically cause the bubble wall to approach a terminal speed  $v_w$ , which is not generally ultra-relativistic. Then the majority of the energy liberated from the phase transition is deposited into heat or the bulk motion of the plasma, and the gravitational waves sourced from the shear stress in the scalar field are negligible. It was argued that, providing the shear stress in the plasma is assumed to be in an infinitesimally thin envelope at the bubble wall, the envelope approximation can once again be applied [14]. Later modelling of bubble collisions introduced a thick fluid shell, and proposed that the velocity field should be Gaussian [17].

Large scale three-dimensional (3D) hydrodynamical simulations [18–20] have dramatically changed the picture. They show that the shear stresses do not disappear with the bubbles, and persist for long after the transition completes, in the form of sound waves. The envelope approximation is not a good description of total gravitational wave production, and predicts incorrectly both the amplitude and shape of the gravitational wave power spectrum. A better picture of the post-collision phase is one of many overlapping counter-propagating sound shells [21].

On the other hand, the envelope approximation does correctly describe the sub-dominant contribution to the power spectrum from the scalar field [22], and analytic studies within the envelope approximation have con-

\* d.cutting@sussex.ac.uk

† m.b.hindmarsh@sussex.ac.uk

‡ david.weir@helsinki.fi

firmed the broken power laws found from numerical simulations [23]. The envelope approximation can also accommodate the idea that fluid shells persist after collision [16, 24].

It is therefore widely believed that the envelope approximation describes the gravitational power in cases where the energy-momentum of the system is dominated by the scalar field, where the system is close to its vacuum state. In this paper, we investigate the quality of the envelope approximation with 3D numerical simulations of a first-order vacuum phase transition.

Classical lattice simulations of a vacuum phase transition have been used to study the power spectrum produced from bubble collisions before [12, 25]. A 1D simulation of the collision of two scalar field bubbles was carried out in Ref. [12]. and used to motivate the envelope approximation in Ref. [26].

In Ref. [25], it was claimed that the power spectrum produced from collisions in 3D simulations with several bubbles was several orders of magnitude smaller than that predicted by the envelope approximation. Furthermore, after the bubbles had finished colliding there appeared to be an additional phase of the transition in which the scalar field continued to oscillate around the true vacuum. During this oscillation phase the power spectrum continued to grow and the peak of the spectrum shifted towards a higher frequency.

Our numerical simulations adopt similar techniques. However, we are able to perform simulations with many more bubbles and higher wall velocities than Ref. [25].

The simulations solve the field equations for a scalar field sourcing gravitational waves in the linear approximation. The transition is modelled by introducing bubbles of the broken phase as initial conditions for the scalar field. This is done in three different ways, modelling three different histories of bubble nucleation. In simultaneous nucleation, we introduce all bubbles at the very start of the simulation. In exponential nucleation simulations, we introduce the bubbles with an exponentially increasing rate per unit volume. In constant nucleation, we introduce the bubbles at a constant rate.

We show power spectra for both the scalar field itself and also the resulting gravitational wave power spectrum for all nucleation types. We find that as we increase the wall velocity to ultra relativistic speeds, the slope of the gravitational wave power spectrum towards the UV becomes steeper than  $k^{-1}$ , and approaches  $k^{-1.5}$ . The peak amplitude and peak location are similar to those predicted by the envelope approximation. We provide a fit for the power spectrum generated from bubble collisions.

We also confirm the existence of a phase after the bubble collisions have finished, during which the scalar field oscillates around the true vacuum and continues to source gravitational waves. This creates an additional bump in the power spectrum that is associated with the mass scale of the scalar field. This continues to grow linearly until very late times, but we show that it has a negligible contribution to the power spectrum in comparison that of

bubble collisions, providing that the mass of the scalar field is smaller than the Planck mass.

In the following section, we recap the dynamics of the scalar field during a vacuum phase transition. This includes the physics of the scalar field during bubble nucleation, expansion, and the eventual collision and oscillation phases of the transition. In Section III we describe how the scalar field sources gravitational waves, and also describe the envelope approximation. The numerical methods used to perform our simulations are discussed in Section IV. Our results are split into two parts; in Section V, we present the behaviour of the scalar field within our simulations, and in Section VI, we analyse the gravitational wave power spectra from our simulations and compare them to the envelope approximation. Our conclusions are listed in Section VII.

## II. DYNAMICS OF VACUUM TRANSITIONS

### A. Scalar field dynamics

In a first-order vacuum transition, bubbles of a new phase of a scalar field nucleate and then expand at ultra-relativistic speeds. At the interface between the two phases a bubble wall forms. In this region the scalar field varies smoothly between the two vacuum expectation values. Upon the collision and subsequently merger of the bubbles the shear stress of the system will source gravitational waves. The shear stress in a vacuum transition is predominantly due to gradients in the scalar field  $\phi$ .

In this work, we study transitions in which the duration of the phase transition is much shorter than the Hubble time  $H_*^{-1}$  when the transition takes place. For such transitions the expansion of the universe can be neglected, and the equation of motion for the scalar field is simply given by

$$\square\phi - V'(\phi) = 0, \quad (1)$$

where  $V(\phi)$  is the effective potential of the scalar field. This is sufficient to investigate the envelope approximation, but may not give accurate results for transitions in which the Universe enters an inflationary phase before bubbles start nucleating.

For these purposes it is sufficient to adopt a simple quartic form for the effective potential,

$$V(\phi) = \frac{1}{2}M^2\phi^2 + \frac{1}{3}\delta\phi^3 + \frac{1}{4}\lambda\phi^4, \quad (2)$$

where the presence of a cubic term allows us to ensure the transition is first-order. The value of the scalar field in the broken phase is then

$$\phi_b = \frac{-\delta + \sqrt{\delta^2 - 4M^2\lambda}}{2\lambda}, \quad (3)$$

with mass

$$M_b = \sqrt{-\delta\phi_b - 2M^2}, \quad (4)$$

The potential difference between the two minima is given by

$$\rho_{\text{vac}} = \frac{1}{12\lambda} (M_b^4 - M^4). \quad (5)$$

By varying the couplings  $M^2$ ,  $\delta$  and  $\lambda$  we are able to change the potential difference  $\rho_{\text{vac}}$  between the two minima of our potential, and also the height of the potential barrier.

The total energy density in the scalar field  $\rho_\phi$  can be split into three components,

$$\rho_\phi = \rho_K + \rho_V + \rho_D, \quad (6)$$

with the kinetic energy density,

$$\rho_K = \frac{1}{2} \dot{\phi}^2, \quad (7)$$

the gradient energy density,

$$\rho_D = \frac{1}{2} (\nabla\phi)^2, \quad (8)$$

and the potential energy density,

$$\rho_V = V(\phi) - V(\phi_b). \quad (9)$$

## B. Bubble nucleation

In a first-order vacuum transition, bubbles nucleate by quantum tunnelling through a potential barrier. This means that they nucleate as critical bubbles, O(4)-symmetric solutions to the Euclidean field equations [7, 8]. When the radius of the critical bubble is much larger than the thickness of the bubble wall the bubble is said to be in the thin wall limit. This occurs when  $\rho_{\text{vac}}$  is much smaller than the height of the potential barrier, or equivalently when the minima are close to degenerate. For our potential the minima are degenerate for

$$\delta = -\frac{3}{\sqrt{2}} M\sqrt{\lambda}. \quad (10)$$

When  $\rho_{\text{vac}}$  is much larger than the height of the potential barrier, the critical bubble is of a similar size to the radius. We leave the study of such bubbles to a later work.

The thin wall solution can be calculated analytically as a function of Euclidean radius,  $r_E = \sqrt{r^2 + \tau^2}$ , where  $r$  is the spatial radius, and  $\tau$  the Euclidean time. In the thin wall limit the scalar field profile of the critical bubble is given by

$$\phi_c(r) = \frac{\phi_b}{2} \left[ 1 - \tanh \left( \frac{r - R_c^{\text{tw}}}{l_0^{\text{tw}}} \right) \right], \quad (11)$$

where  $l_0$  is thickness of the bubble wall, which is given in the thin wall limit by

$$l_0^{\text{tw}} = \frac{2}{\sqrt{V''(\phi_b)}}, \quad (12)$$

and  $R_c^{\text{tw}}$  is the radius of the critical bubble. The radius of the critical bubble can be estimated by extremising the approximate expression for the Euclidean action

$$S_4 = 2\pi^2 R^3 \sigma^{\text{tw}} - \frac{\pi^2}{2} R^4 \rho_{\text{vac}}, \quad (13)$$

where

$$\sigma^{\text{tw}} = \frac{M^3}{3\lambda}, \quad (14)$$

is interpreted as the surface tension of the bubble. Then the critical radius is

$$R_c^{\text{tw}} = \frac{3\sigma^{\text{tw}}}{\rho_{\text{vac}}}. \quad (15)$$

At the point of time symmetry  $\tau = 0$ , the energy liberated from the vacuum is equal to the energy in the wall. Furthermore, the outward force on the bubble wall due to the pressure difference  $\rho_{\text{vac}}$  is equal and opposite to that caused by the surface tension.

Once the bubble has nucleated, the solution is found by the analytic continuation to Minkowski space, so that

$$\phi(r, t) = \begin{cases} \phi_c(\sqrt{r^2 - t^2}), & r > t, \\ \phi_b, & r \leq t. \end{cases} \quad (16)$$

The probability of nucleating a bubble per unit volume per unit time  $p(t)$  is given by [8]

$$p(t) = p_n \exp(-S_4). \quad (17)$$

Very often the Euclidean action decreases slowly in time due to a change in temperature or a background field. Then we may write

$$p(t) = p_f \exp[\beta(t - t_f)], \quad (18)$$

where  $\beta = -d \ln p(t)/dt|_{t_f}$  and  $t_f$  is the time at which the fraction of the universe in the symmetric phase is  $h(t_f) = 1/e$  [27]. The bubble number density can be shown to be

$$n_b = \frac{1}{8\pi} \frac{\beta^3}{v_w^3}, \quad (19)$$

where in the vacuum case  $v_w$  is very close to unity. We will refer to this case as exponential nucleation.

It is also possible that  $S_4(t)$  has a minimum which is reached at time  $t_0$  before a transition completes. Then the probability of nucleating a bubble per unit volume could be approximated by

$$p(t) = p_0 \exp[-\frac{1}{2}\beta_2^2(t - t_0)^2], \quad (20)$$

where  $\beta_2 = \sqrt{S''(t_0)}$ . Nucleation is then concentrated around time  $t_0$  [28]. The bubble density is

$$n_b = \sqrt{2\pi} \frac{p_0}{\beta_2}. \quad (21)$$

We will refer to this case as simultaneous nucleation.

The last possibility we consider is if  $S_4(t)$  tends to a constant (for a model with a constant nucleation rate see Ref. [29]). We would then expect bubbles to nucleate at a constant rate

$$p(t) = p_c, \quad (22)$$

for which

$$n_b = \frac{1}{4} \left( \frac{3}{\pi} \right)^{1/4} \Gamma \left( \frac{1}{4} \right) \left( \frac{p_c}{v_w} \right)^{3/4}. \quad (23)$$

We will refer to this as constant nucleation.

### C. Bubble growth

If we consider a thin wall bubble then we can obtain an expression for the evolution of the bubble simply by considering energy conservation. The energy in the static bubble wall per unit area is simply  $\sigma^{\text{tw}}$ . Then if the bubble wall is expanding at some velocity  $v_w$ , the energy per unit area is given by  $\sigma^{\text{tw}}\gamma$  where  $\gamma$  is the wall's Lorentz factor. The total energy of an expanding bubble with radius  $R$  is then [7, 8]

$$E_{\text{bub}} = 4\pi R^2 \sigma^{\text{tw}} \gamma - \frac{4}{3}\pi R^3 \rho_{\text{vac}}, \quad (24)$$

where we can define  $R$  to be the point in the scalar field profile such that  $\phi(R) = \phi_b/2$ . As we are considering vacuum decay, we expect  $E_{\text{bub}} = 0$ . We therefore obtain that, for a bubble of radius  $R$ , the Lorentz factor of the bubble wall is given by

$$\gamma(R) = \frac{R\rho_{\text{vac}}}{3\sigma^{\text{tw}}} = \frac{R}{R_c^{\text{tw}}}. \quad (25)$$

We expect Eq. (25) to apply outside the thin wall limit by recalling that the solution of the classical field equations is simply the analytic continuation of the O(4)-symmetric bounce solution [7]. Then any point in the field profile of the critical bubble we define to be the critical radius  $R_c$  will expand out with a hyperboloid motion satisfying

$$R^2(t) - t^2 = R_c^2, \quad (26)$$

which is equivalent to Eq. (25).

### D. Bubble collision and oscillation phase

For bubbles with thin walls, after collision part of the overlap region rebounds and returns towards the false

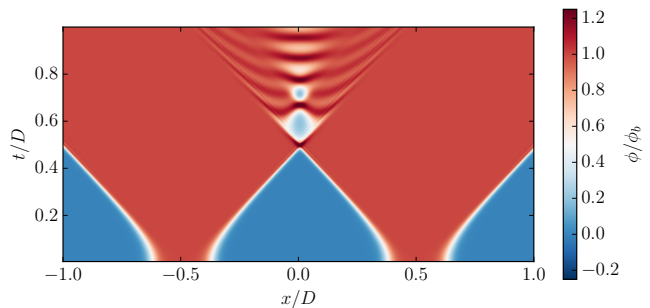


FIG. 1. Values of the scalar field along the collision axis during a two bubble collision where  $R_c M = 7.15$ . Here the  $x$  axis is the collision axis which connects the two bubble centres. The  $y$  axis is time since the nucleation of the bubbles. The bubbles are separated by a distance  $D$ . This figure can be compared with Fig. 1 of [30] and Fig. 7 of [31].

vacuum [30, 31]. In Fig. 1, we plot the variation during a collision of the scalar field along the collision axis connecting two bubble centres. At the collision point it can be seen that the scalar field oscillates between the true and false vacuum. These large amplitude oscillations are the source of scalar radiation moving at close to the speed of light, and can also induce rapid production of light particles through parametric resonance [32]. This rebounding and oscillation phase is something that is not accounted for within the envelope approximation. Away from the thin wall limit, the scalar field in the overlap region is not able to return to the false vacuum, and instead will just oscillate around the true vacuum [31].

After this stag, the scalar field continues to oscillate around the true vacuum with large amplitude oscillations. In the absence of other interactions, scalar fields take a substantial time to thermalise [33–35].

## III. GRAVITATIONAL WAVES FROM A PHASE TRANSITION

In order to calculate the gravitational wave power spectrum, we need to find the transverse traceless (TT) metric perturbations  $h_{ij}^{TT}$  where

$$\square h_{ij}^{TT} = 16\pi G T_{ij}^{TT}, \quad (27)$$

and  $T_{ij}^{TT}$  is the transverse traceless projection of the energy-momentum tensor,

$$T_{\mu\nu} = \partial_\mu \phi \partial_\nu \phi - \eta_{\mu\nu} \left( \frac{1}{2} (\partial\phi)^2 + V(\phi) \right), \quad (28)$$

where  $\eta_{\mu\nu}$  is the Minkowski metric. The energy density in the gravitational waves can be defined as

$$\rho_{\text{gw}}(\mathbf{x}, t) = \frac{1}{32\pi G} \dot{h}_{ij}^{TT} \dot{h}_{ij}^{TT}. \quad (29)$$

Note that an average over many wavelengths and periods may be needed in order to reduce fluctuations in this quantity.

We introduce an auxiliary tensor  $u_{ij}$  which satisfies [36]

$$\square u_{ij} = 16\pi G(\partial_i\phi)(\partial_j\phi). \quad (30)$$

To obtain  $h_{ij}^{TT}$  we use the projector  $\Lambda_{ij,lm}$  on  $u_{ij}$  in momentum space,

$$h_{ij}^{TT}(\mathbf{k}, t) = \Lambda_{ij,lm}(\mathbf{k})u_{lm}(\mathbf{k}, t), \quad (31)$$

where

$$\Lambda_{ij,lm}(\mathbf{k}) = P_{im}(\mathbf{k})P_{jl}(\mathbf{k}) - \frac{1}{2}P_{ij}(\mathbf{k})P_{lm}(\mathbf{k}), \quad (32)$$

and

$$P_{ij}(\mathbf{k}) = \delta_{ij} - \hat{k}_i\hat{k}_j. \quad (33)$$

We then define the spectral density of the time derivative of the metric perturbations  $P_{\dot{h}}$  as

$$\langle \dot{h}_{ij}^{TT}(\mathbf{k}, t)\dot{h}_{ij}^{TT}(\mathbf{k}', t) \rangle = P_{\dot{h}}(\mathbf{k}, t)(2\pi)^3\delta(\mathbf{k} + \mathbf{k}'). \quad (34)$$

Therefore the power spectrum of gravitational wave energy density is

$$\frac{d\rho_{\text{gw}}}{d\ln(k)} = \frac{1}{32\pi G} \frac{k^3}{2\pi^2} P_{\dot{h}}(\mathbf{k}, t), \quad (35)$$

and by dividing through by the critical energy density  $\rho_c$  we obtain the power spectrum of the gravitational wave energy density parameter

$$\frac{d\Omega_{\text{gw}}}{d\ln(k)} = \frac{1}{32\pi G\rho_c} \frac{k^3}{2\pi^2} P_{\dot{h}}(\mathbf{k}, t). \quad (36)$$

### A. Collision Phase: envelope approximation

In the envelope approximation [13], the bubble walls are treated as infinitely thin, expanding with speed  $v_w$ , and containing all the vacuum energy released by the transition. The overlap region of collided bubbles are ignored, and the gravitational waves from shear stress “envelope” calculated. The resulting spectrum was re-computed with many more bubbles in Ref. [15], and again in Ref. [16], for an exponential nucleation rate in both cases.

The gravitational wave power spectrum is well approximated by a broken power law

$$\frac{d\Omega_{\text{gw}}^{\text{env}}}{d\ln(k)} = \Omega_{\text{p}}^{\text{env}} \frac{(a+b)\tilde{k}^b k^a}{b\tilde{k}^{(a+b)} + ak^{(a+b)}}, \quad (37)$$

with power law exponents  $a$  and  $b$ , peak amplitude  $\Omega_{\text{p}}^{\text{env}}$  and peak wavenumber  $\tilde{k}$ . The peak amplitude was found to be

$$\Omega_{\text{p}}^{\text{env}} \simeq \frac{0.44v_w^3}{1 + 8.28v_w^3} \left( \frac{H_*}{\beta} \right)^2 (\kappa_\phi\Omega_{\text{vac}})^2, \quad (38)$$

where the Hubble rate at the time of the transition  $H_*$ , the vacuum energy density parameter  $\Omega_{\text{vac}} = \rho_{\text{vac}}/\rho_c$  and the bubble wall velocity  $v_w$ . The peak frequency was estimated to be

$$\tilde{k}/\beta \simeq \frac{1.96}{1 - 0.051v_w + 0.88v_w^2}. \quad (39)$$

The efficiency factor  $\kappa_\phi$  measures the fraction of vacuum energy that is converted to stress energy localised at the bubble wall. We define it as

$$\kappa_\phi = \frac{2\rho_D}{\rho_{\text{vac}} - \rho_V}. \quad (40)$$

For a vacuum phase transition  $\kappa_\phi \simeq 1$ .

The exponent for the broken power law on the low frequency side is expected to be  $a = 3$  due to causality [37]. In Ref. [16], the power law exponents were found to be  $a = 2.9$  and  $b = 0.9$  for  $v_w \simeq 1$  and  $a = 2.95$  and  $b = 1$  for  $v_w \ll 1$ . Furthermore, in Ref. [22], the envelope approximation was compared to lattice simulations of a scalar field with frictional effects chosen such that the bubble walls asymptotes a constant speed  $v_w = 0.44$ . The gravitational wave power spectrum generated by stress energy in the scalar field was found to agree well with the envelope approximation. The power law exponents for the envelope approximation in this study were found to be  $a = 2.98 \pm 0.02$  and  $b = 0.62 \pm 0.05$  [22].

There is also some analytical understanding of the power spectrum produced under the envelope approximation. In Ref. [23], it is shown that the two point correlator of the energy-momentum tensor can be expressed as a 1-dimensional integral under the envelope approximation, also producing a broken power law with exponents  $a = 3$  and  $b = 1$ .

It should be noted that while typically in a thermal phase transition friction effects from the plasma cause  $v_w$  to approach a constant, in a vacuum phase transition the bubble wall accelerates until collision with  $v_w \rightarrow 1$  and  $\gamma \rightarrow \infty$ . In this current work we shall check whether the formula is a good fit in the case where the bubble wall continues to accelerate until collision, reaching ultra-relativistic velocities.

### B. Oscillation phase

Previous simulations of a vacuum first-order phase transition have observed that after all the bubble collisions have completed, the scalar field continues to oscillate, and the production of gravitational radiation continues [25].

The contribution to the gravitational wave power spectrum from this oscillation phase was seen to dominate that of the bubble collisions by more than an order of magnitude. The peak frequency moved towards the UV by an order of magnitude during the oscillation phase.

Providing the oscillations in the scalar field are non-linear [38] we would expect them to be a continuous

$R_c M$	$l_0 M$	$\delta/M$	$\lambda$	$ \phi_b/M$	$\rho_{\text{vac}}/M^4$	$\sigma^{\text{tw}}/M^3$	$l_0^{\text{tw}} M$	$R_c^{\text{tw}} M$
7.15	1.71	-1.632	0.5	2.45	0.495	2/3	1.42	4.04
14.3	1.83	-1.56	0.5	2.22	0.189	2/3	1.65	10.6
28.8	1.91	-1.528	0.5	2.11	0.0809	2/3	1.81	24.7

TABLE I. Critical radii  $R_c$  and wall thicknesses  $l_0$  that are used in our simulations. For each of these we give the potential parameters  $\delta$  and  $\lambda$  used to derive them, the broken phase value of the scalar field  $\phi_b$  and the vacuum energy density  $\rho_{\text{vac}}$ . We also list the surface tension  $\sigma^{\text{tw}}$ , wall thickness  $l_0^{\text{tw}}$  and critical radius  $R_c^{\text{tw}}$  as derived from the thin wall approximation.

source of gravitational waves, similar to acoustic waves in a thermal phase transition [19]. Eventually Hubble friction would damp out the oscillations.

A further goal of the current work is to investigate if we also see the growth of the gravitational wave power spectrum during an oscillation phase in our simulations.

#### IV. METHODS

To perform our study we perform a series of simulations solving the partial differential equations (1) and (30) on a 3-dimensional lattice, using code built on the open source C++ library LATfield2 [39]. To compute derivatives we use a central finite difference method. For the Laplacian we use the minimal 7-point stencil made up of a central point and then an additional 2 points in each dimension. We choose our timestep  $\Delta t$  and lattice spacing  $\Delta x$  such that  $\Delta t = 0.2\Delta x$ . We advance in timestep by using the leapfrog algorithm.

Our simulations are on a cubic grid with total volume  $\mathcal{V} = (L\Delta x)^3$ , and periodic boundary conditions. We begin each simulation by nucleating at least one bubble at the simulation time  $t = 0$ . The total number of bubbles nucleated by the end of the simulation is given by  $N_b$ .

We use a shooting method to find the critical profile for specific values of  $M^2$ ,  $\delta$  and  $\lambda$ . We choose three profiles to simulate and give the parameters for these in Table I. The resulting field profiles are modelled well by Eq. (11) with values for  $R_c$  and  $l_0$  given in the first two columns. Note that they differ from the thin wall values due to the finite size of the bubble.

The value of  $R_c$  is given by the location in the numerical profile at which

$$\phi_c(R_c) = \frac{\phi_b}{2}. \quad (41)$$

Similarly,  $l_0 = r^+ - r^-$  where

$$\phi_c(r^\pm) = \frac{\phi_b}{2} (1 - \tanh(\pm 1/2)). \quad (42)$$

We nucleate bubbles with a critical profile inside our numerical simulation. Before nucleating the  $N$ th bubble we check that, for all  $n < N$ , the distance between

the  $N$ th and  $n$ th bubble centres  $r_n$  obeys the following relation

$$r_n^{\text{sep}} > R_c + \sqrt{R_c^2 + (t - t_n)^2}, \quad (43)$$

where  $t_n$  is the time at which the  $n$ th bubble nucleated. Providing this is satisfied for all bubbles, we nucleate a bubble by modifying  $\phi \rightarrow \phi'$ , where

$$\phi'(r) = \sqrt{\phi^2(r) + \phi_c^2(r)}. \quad (44)$$

We evolve the auxiliary metric tensor  $u_{ij}$  in real space at every timestep. At routine intervals we perform a Fourier transform of  $\dot{u}_{ij}$ , and then project the result according to Eq. (31) to find  $\dot{h}_{ij}^{TT}(\mathbf{k}, t)$ . From this we then calculate the gravitational wave power spectrum. It should be noted that in our units  $G = 1$ , though in general we plot quantities that do not depend on  $G$ .

We can nucleate bubbles simultaneously at the start of the simulation, or indeed with a nucleation rate throughout its duration. In order to compare with earlier studies using the envelope approximation, we nucleate bubbles with an exponentially increasing nucleation rate, using the algorithm given in Ref. [27]. Then the probability of nucleating a bubble per unit volume and time is given by Eq. (18). The parameters of the simultaneous nucleation runs are listed in Table II, and those of the exponential nucleation runs in Table III. We also perform two constant nucleation runs to check that this type of nucleation is consistent with our other results. The parameters of the constant nucleation runs are given in Table IV.

We also wish to study the gravitational wave power spectrum produced after the bubble collision phase is completed. In order to do this, we can simply turn on the evolution of  $u_{ij}$  once the bubbles have finished colliding. We employ this approach for a series of simultaneous nucleation simulations listed in Table V.

There are a number of length scales within our simulation. The largest physical length scale within our system is the average separation between bubbles  $R_*$ . This is simply given by

$$R_* = \left( \frac{\mathcal{V}}{N_b} \right)^{1/3}. \quad (45)$$

Much smaller than this length scale is the radius of the critical bubble  $R_c$ , and the critical bubble wall width  $l_0$ . The critical bubble wall width is associated with the scalar field mass in the broken phase. Smaller still is the length scale of the Lorentz contracted bubble walls. We define  $\gamma_* = R_*/2R_c$  which is the expected Lorentz factor for a bubble with diameter  $R_*$ , and then define  $l_* = l_0/\gamma_*$  as the width of the Lorentz contracted bubble wall with a diameter of  $R_*$ . It is crucial that we have a good resolution of the bubble walls up until they collide, and as such we need our lattice spacing  $\Delta x \ll l_*$ . Note that by obtaining different values of  $R_c$  we can vary  $R_*$  while keeping  $\gamma_*$  the same.

In most vacuum phase transitions we expect bubbles to expand to many times the size of the critical bubble, and

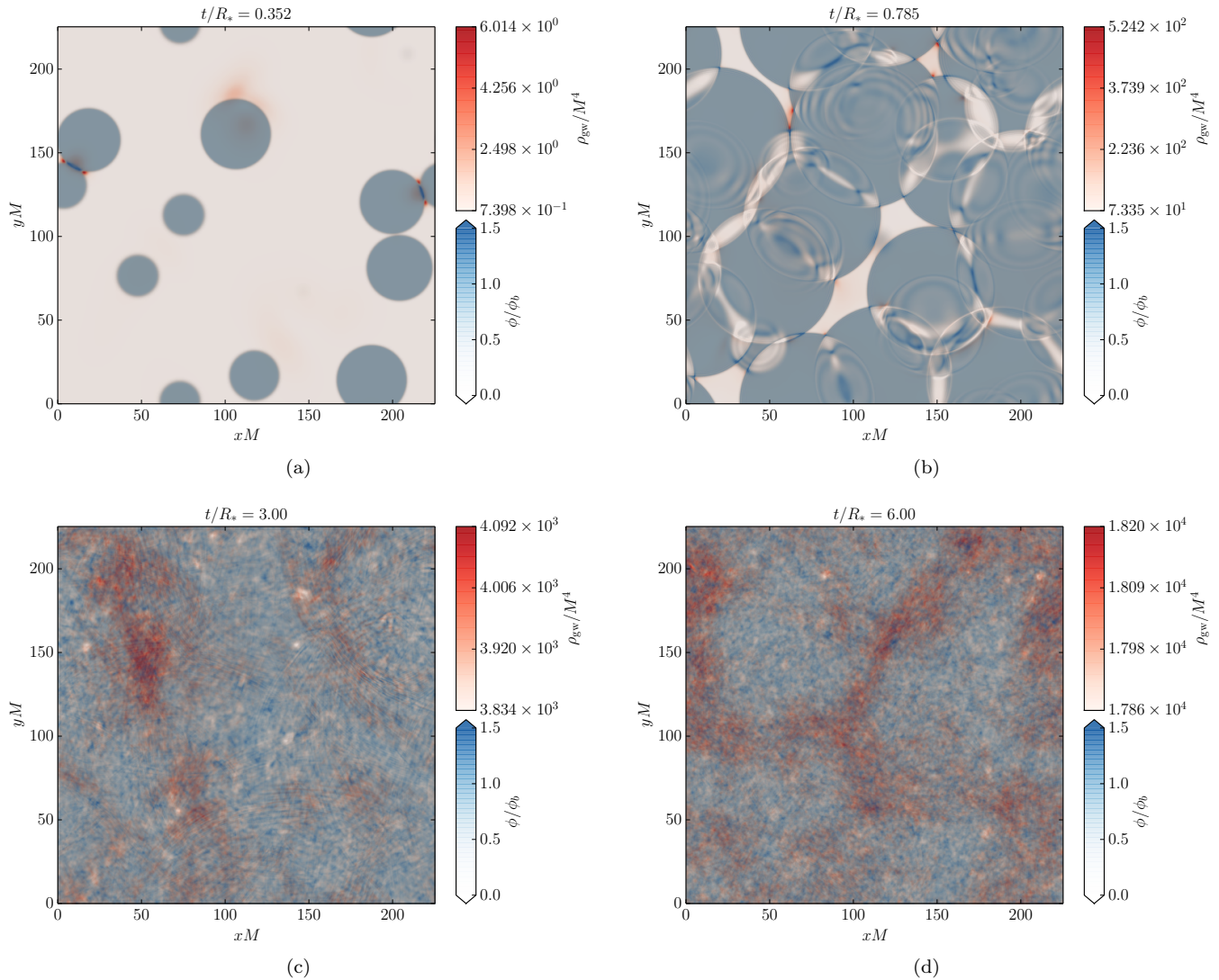


FIG. 2. Slices through a simultaneous nucleation simulation with parameters  $R_c M = 7.15$ ,  $N_b = 64$  and  $R_* M = 56.32$  showing the expansion (a), collision (b), and oscillatory (c and d) phase of the scalar field. The scalar field value is shown in blue, and the gravitational wave energy density is shown in red. Note that the range of the colourbar for the gravitational wave energy density changes for each plot. During the oscillatory phase the gravitational wave energy density becomes very uniform and the “hotspots” are deviations on the sub percent level. The full set of parameters for this run is shown in Table II. A movie based on this simulation is included in the supplemental material.

therefore up to very high Lorentz factors. We also would like to have many bubbles within our simulation box to obtain an accurate ensemble. Hence, we need sufficiently large lattices to separate the scales

$$\Delta x \ll l_* \ll l_0 \lesssim R_c \ll R_* \ll L \Delta x. \quad (46)$$

It is not possible to perform a simulation in which we achieve a realistic value for  $\gamma_*$  and a correct separation of scales. Instead, we perform multiple simulations with increasing values of  $\gamma_*$  to attempt to identify a trend as  $\gamma_* \rightarrow \infty$ .

For simulations with a given nucleation rate, we typically expect the first bubble nucleated to grow to a larger size than bubbles nucleated later, and so the wall of the

first bubble when it collides will have  $\gamma$  greater than  $\gamma_*$ . Its bubble wall at collision will therefore be thinner than  $l_*$ . This effect is particularly pronounced for simulations with an exponential nucleation rate where the first bubble nucleated often grows to be many times larger than the subsequent bubbles at collision time. For a simultaneous nucleation run the diameters of the bubbles will be more closely distributed around  $R_*$ , and so the thinnest wall at collision will be much closer to  $l_*$ .

For an exponential nucleation rate simulation we need a much finer lattice spacing in comparison to a simultaneous nucleation simulation with the same  $l_*$ . In practice, reducing the lattice spacing is too expensive and for large volumes we become unable to trust our results due to bad

$R_c M$	$\gamma_*$	$R_* M$	$N_b$	$L \Delta x M$	$L$	$\Delta x M$	$\gamma_*^{\text{lat}}$
7.15	1.97	28.2	8	56.32	128	0.44	1.85
7.15	1.97	28.2	64	112.64	256	0.44	1.85
7.15	1.97	28.2	512	225.28	512	0.44	1.85
7.15	1.97	28.2	4096	450.56	1024	0.44	1.85
7.15	3.94	56.3	8	112.64	512	0.22	3.37
7.15	3.94	56.3	64	225.28	1024	0.22	3.37
7.15	3.94	56.3	512	450.56	2048	0.22	3.37
7.15	3.94	56.3	4096	901.12	4096	0.22	3.37
7.15	7.88	113.	8	225.28	2048	0.11	5.65
14.3	1.97	56.3	512	450.56	1024	0.44	1.87
28.8	1.96	113.	512	901.12	2048	0.44	1.89

TABLE II. Parameters of the simultaneous nucleation simulations used within this paper. Listed here for each run is the critical radius  $R_c$ , typical Lorentz factor at collision  $\gamma_*$ , average bubble separation  $R_*$ , number of bubbles  $N_b$ , number of lattice points  $L^3$ , lattice spacing  $\Delta x$ , and effective  $\gamma_*$  as found on the lattice  $\gamma_*^{\text{lat}}$ . Not given here are simulation runs where the metric perturbations are turned on after the bubbles have finished colliding, see Table V.

$R_c M$	$\gamma_*$	$\beta/M$	$R_* M$	$N_b$	$L \Delta x M$	$L$	$\Delta x M$	$\gamma_*^{\text{lat}}$
7.15	1.97	0.180	28.2	8	56.32	128	0.44	1.85
7.15	1.92	0.180	27.5	69	112.64	256	0.44	1.81
7.15	1.96	0.180	28.0	522	225.28	512	0.44	1.84
7.15	3.94	0.0625	56.3	8	112.64	512	0.22	3.37
7.15	4.09	0.0625	58.5	57	225.28	1024	0.22	3.55
7.15	7.57	0.0290	108.	9	225.28	2048	0.11	5.58

TABLE III. Parameters of the exponential nucleation simulations used within this paper.

$R_c M$	$\gamma_*$	$p_c/M^4$	$R_* M$	$N_b$	$L \Delta x M$	$L$	$\Delta x M$	$\gamma_*^{\text{lat}}$
7.15	3.94	$1.50 \times 10^{-7}$	56.3	64	225.28	1024	0.22	3.37
7.15	4.09	$1.50 \times 10^{-7}$	56.3	510	450.56	2048	0.22	3.37

TABLE IV. Parameters of the constant nucleation simulations used within this paper.

$R_c M$	$\gamma_*$	$R_* M$	$N_b$	$L \Delta x M$	$L$	$\Delta x M$	$\gamma_*^{\text{lat}}$
7.15	3.94	56.3	64	225.28	1024	0.44	3.37
14.3	1.97	56.3	512	450.56	1024	0.44	1.87
14.3	3.94	113.	8	225.28	1024	0.22	3.34
28.8	1.96	113.	64	450.56	1024	0.44	1.89

TABLE V. Parameters of the simultaneous nucleation simulations where the metric perturbations are turned on at  $t/R_* = 2.0$  at which point most of the bubbles have finished colliding. This is in order to see the shape of the power spectrum due to scalar field radiation during the oscillation phase.

energy conservation.

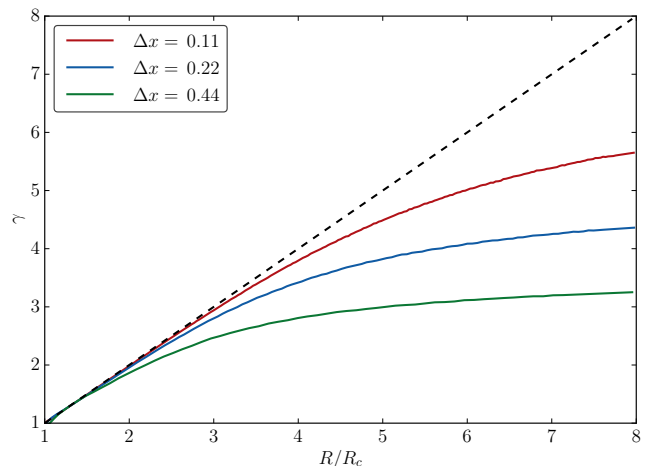


FIG. 3. The Lorentz factor  $\gamma$  of the bubble wall for different values lattice spacings plotted against the radius of the bubble in units of the critical radius. This is for a bubble with  $R_c M = 7.15$ . The dashed black line shows  $\gamma = R/R_c$ .

## V. RESULTS: SCALAR FIELD

As described in the previous section, the scalar field evolution can roughly be split into three stages, expansion, collision, and oscillation. Slices through a simultaneous nucleation simulation volume are shown in Fig. 2. During collision, we see many regions in which the scalar field is rebounding into the symmetric phase as described in Section IID. During the oscillation phase the scalar field becomes more homogeneous on large scales while the scalar field continues to oscillate on small wavelengths. This persists as long as the simulations run, for times that are many multiples of  $R_*$ .

In order to test for lattice effects, we study single bubbles, whose Lorentz factors should be related to their radius through Eq. (25). We find the volume by counting the number of lattice sites with  $\phi > \phi_b$ , and then from this we are able to deduce the bubble radius  $R$  and the Lorentz factor of the wall  $\gamma$ .

We plot  $\gamma$  against  $R$  in Fig. 3. The lattice effects are easy to see, as  $\gamma$  is highly sensitive to small changes in velocity when  $v_w \rightarrow 1$ . The bubble wall is stopped from contracting beyond a width which is representable on the lattice, and the bubble wall is unable to increase its velocity. The energy that is lost is transferred to small wavelength oscillations that follow behind the bubble wall. This effect has been seen previously in accelerating kinks on a lattice [40, 41].

If the deviation of  $\gamma$  from its theoretical value becomes sufficiently large then this can be associated with loss of energy conservation.

We plot the energy densities over time for a simultaneous nucleation phase transition in Fig. 4. As the bubbles expand the potential energy drops steeply and the kinetic and gradient energies increase. Initially the gradient en-



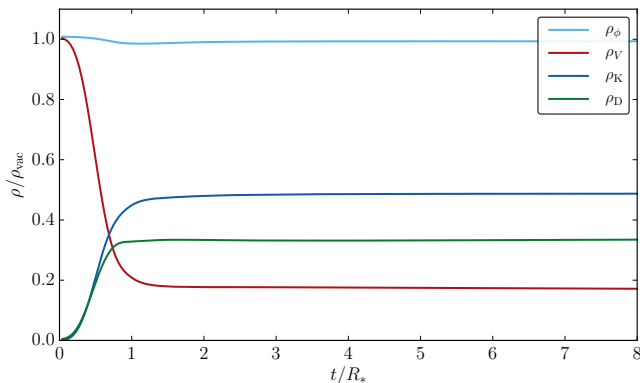


FIG. 4. Energy densities in the scalar field over time for a simultaneous nucleation run with  $R_c M = 7.15$ ,  $R_* M = 56.3$  and  $N_b = 4096$ . The full set of parameters for this run is shown in Table II.

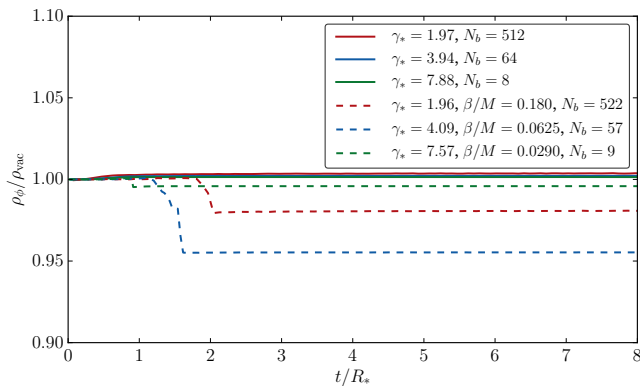


FIG. 5. Energy conservation for several simulations of the same physical volume. Runs with exponential nucleation are plotted with dashed lines, and simultaneous nucleation runs are shown with solid lines. See Tables II and III for the full set of parameters of each run.

ergy and kinetic energy are roughly equal but when the bubbles begin to collide the kinetic energy becomes larger than the gradient energy. Shortly after the phase transition enters the oscillation stage, with  $\rho_V \neq 0$ .

The energy conservation for a series of simulations with  $L\Delta x = 225.28$  is given in Fig. 5. We can see that energy conservation is substantially better in the simultaneous nucleations in comparison to the exponential nucleation runs. This is what we expected due to the biggest bubble/thinnest wall effect mention in section IV. These are the largest volume simulation runs for exponential nucleation, and so have the worst energy violation of all simulations performed. Even in the worst case, energy conservation violation is still kept to  $\lesssim 5\%$ .

To monitor energy conservation in our multi-bubble simulations, we define a new parameter  $\gamma_*^{\text{lat}}$  which is the numeric value found for  $\gamma$  on the lattice when the bubble radius is  $R = R_*$ . This new parameter is listed for all simulation runs in their respective tables.

The power spectrum of the scalar field  $\mathcal{P}_\phi$  can inform us about the length scales of the shear stresses sourcing gravitational waves. We plot  $\mathcal{P}_\phi$  during the expansion, collision and oscillation phases for both a simultaneous and exponential nucleation phases run in Fig. 6. During expansion and collision  $\mathcal{P}_\phi$  is peaked around  $R_*$ . During the oscillation phase  $\mathcal{P}_\phi$  shifts so that its maximum is at a higher wavelength, closer to the scale associated with  $l_0$ . This can be understood as the structure of bubbles disappearing and being replaced with oscillating features around the mass scale of the scalar field.

The main differences in  $\mathcal{P}_\phi$  between the simultaneous and exponential nucleation runs are during the expansion and collision phases. Identical bubbles are all spawned at the start of the simultaneous nucleation run, and so  $\mathcal{P}_\phi$  has a larger magnitude at  $t/R_* = 0.0$ , and shows the characteristic “ringing” of the single-bubble power spectrum. These bubbles then expand in a uniform way, their geometries differentiating from each other only upon collision with another bubble. Comparatively, as more bubbles are spawned during the exponential nucleation run  $\mathcal{P}_\phi$  becomes smoother on large scales and noisier on small scales as bubbles of varying sizes appear. The collision phase also lasts longer, and the distribution of bubbles is not as homogeneous as in a simultaneous nucleation run.

If we plot the late time scalar field power spectrum together on the same graph we can clearly see that during the oscillation phase the simultaneous and exponential nucleation runs settle into similar states. We do this for several values of  $\gamma_*$  in Fig. 7. In all cases, the scalar power spectra settle into similar states apart from lattice effects in the UV.

## VI. RESULTS: GRAVITATIONAL WAVES

### A. Simultaneous nucleation

In Fig. 2, we also show in shades of red the gravitational wave energy density  $\rho_{\text{gw}}(\mathbf{x}, t)$  sourced by the scalar field. To obtain  $\rho_{\text{gw}}$  in real space we first perform the Fourier transform of  $\dot{u}_{ij}$ , then project this to obtain  $\dot{h}_{ij}^{TT}$  in  $k$ -space. Finally we perform the inverse Fourier transform to find  $\dot{h}_{ij}^{TT}$  in real space. From this we then calculate  $\rho_{\text{gw}}(\mathbf{x}, t)$  using Eq. (29).

We can clearly see from Fig. 2 that during the collision phase hotspots in  $\rho_{\text{gw}}$  are located in regions where bubbles are colliding. These are the locations where the spherical symmetry of the expanding bubbles is broken. During the oscillation phase the gravitational wave energy density becomes largely homogeneous with fluctuations on the percent level, though gravitational waves continue to be sourced.

In Fig. 8, we plot the gravitational wave power spectrum at several times over the duration of a simultaneous nucleation simulation with  $\gamma_* \simeq 4$ . As the bubbles begin to collide we begin to see a peak in the spectrum emerging near  $k = 2\pi/R_*$ , with a power law fall-off towards

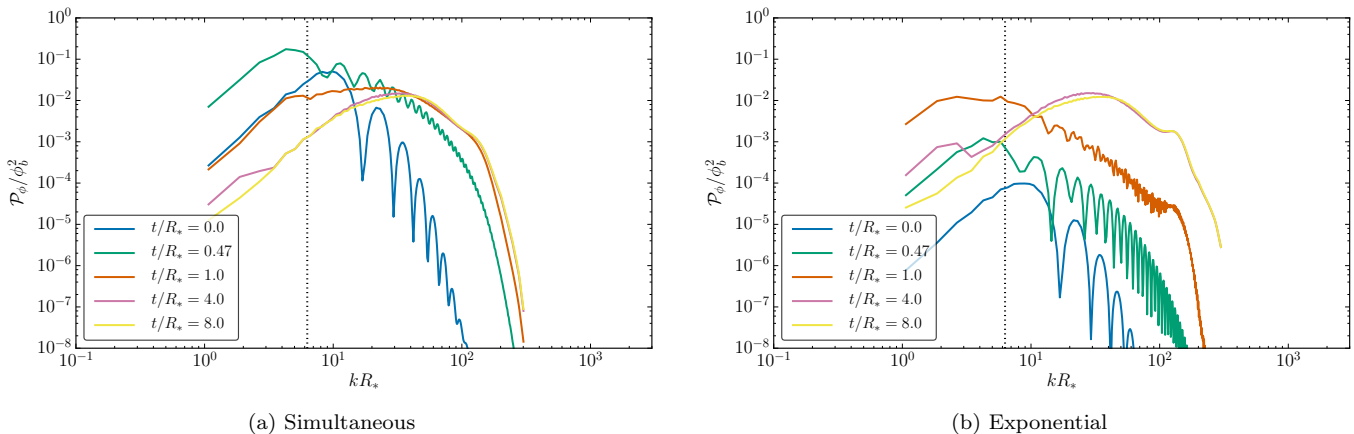


FIG. 6. Scalar power spectra for simultaneous (left) and exponential (right) nucleation runs. Both simulations have  $R_c M = 7.15$ . The left plot has  $N_b = 512$  and  $\gamma_* = 1.97$ , while the right plot has  $N_b = 522$  and  $\gamma_* = 1.96$ . The full set of parameters of each run can be extracted from Tables II and III. The initial configuration of the scalar field is seen at  $t/R_* = 0$ . The bubble expansion phase is seen for  $t/R_* = 0.47$ . The spectrum during bubble collision is seen at  $t/R_* = 1.0$ . The late time power spectrum after bubbles have collided is then shown at  $t/R_* = 4.0$  and  $t/R_* = 8.0$ . The vertical black dotted line denotes  $k = 2\pi/R_*$ .

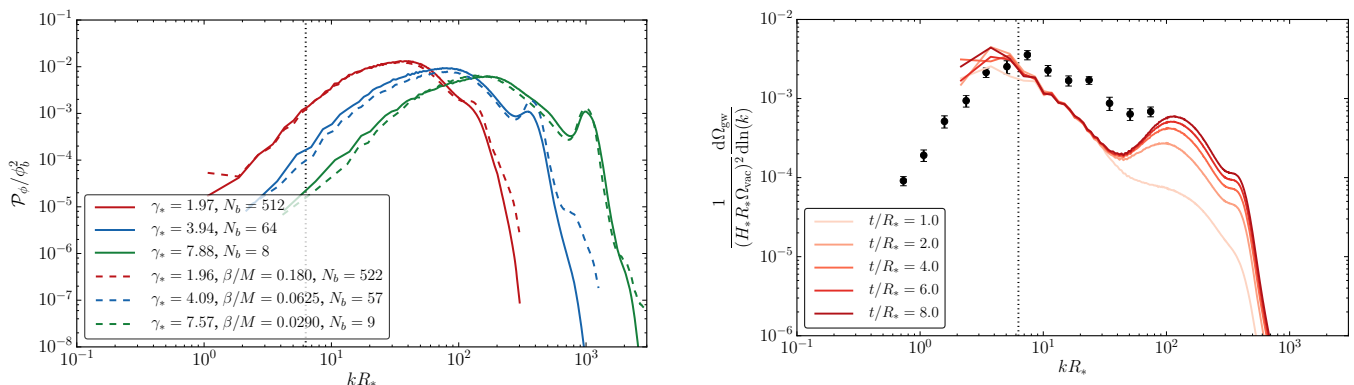


FIG. 7. Comparison of the late time scalar power spectrum at  $t/R_* = 8.0$  for both simultaneous (solid lines) and exponential (dashed lines) nucleation runs. All runs use bubbles with  $R_c M = 7.15$ . See Tables II and III for the full set of parameters of each run.

the UV. For this simulation we do not have a sufficient separation between  $R_*$  and  $L\Delta x$  to estimate the power law towards the IR. As the collision phase completes this peak and the power law towards the IR persists, but a second peak associated with a much smaller length scale continues to grow. This second peak is due to gravitational waves sourced from oscillations in the scalar field with wavelengths close to the inverse mass of the scalar field.

In the same figure, we also plot the results of a numerical calculation in the envelope approximation, as detailed in [22], using the same bubble nucleation locations. The peak power in our simulation is closely reproduced by the envelope calculation, although the envelope calcula-

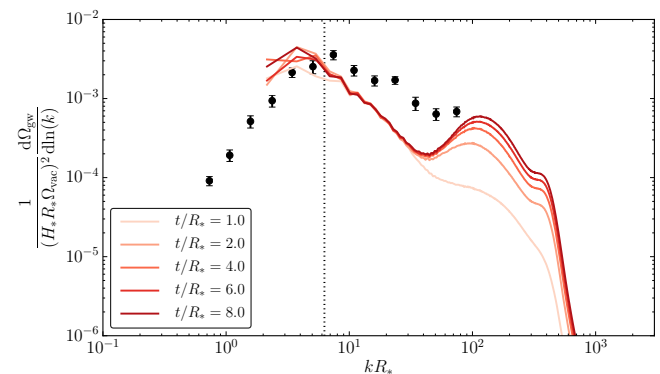


FIG. 8. The gravitational wave power spectrum for the simultaneous nucleation run with  $R_c M = 7.15$ ,  $N_b = 64$  and  $\gamma_* = 3.94$  listed in Table II. The vertical black dotted line marks where  $k = 2\pi/R_*$ . The black data points are the results for running a simulation with the envelope approximation with the same bubble locations and nucleation times.

tion predicts that the peak is at higher frequency. The power law towards the UV is somewhat steeper in the numerical simulations than in the envelope calculation.

We can show that the frequency of peak power is associated with the length scale of  $R_*$ , whereas the bump in the UV is associated with the length scale  $l_0$ . In Fig. 9, we plot the power spectra for three runs with different values of  $R_c$  and  $R_*$  but the same  $\gamma_*$ . It can be seen that the power peaks at  $kR_* \simeq 3$ , with a secondary peak at  $kl_0 \simeq 3$ .

In a realistic transition, the separation between  $R_*$  and  $l_0$  will be many orders of magnitude, and we would expect the UV peak will be greatly suppressed due to the fall-off of the power spectrum with increasing  $k$ . We will

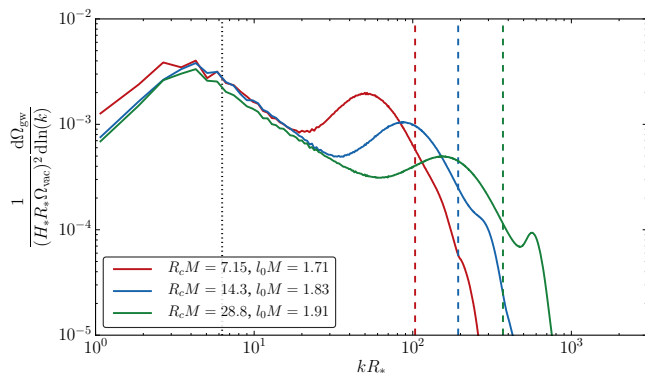


FIG. 9. Gravitational wave power spectrum for several runs with different critical radius  $R_c$  and  $R_*$ . For each simulation the power spectra have been averaged over the interval  $2.5 \leq t/R_* \leq 8.0$ . All simulations shown have the same number of bubbles  $N_b = 512$  and  $\gamma_* \simeq 2$ , with the full set of parameters listed in Table II. We also plot the length scale associated with  $R_*$  as the vertical black dotted line, and the corresponding length scale for the initial wall width  $l_0$  for each simulation as coloured dashed lines.

estimate how large it can grow below.

Note that the power spectrum fluctuates due to the oscillations in the individual Fourier modes. In order to minimise this effect, in some plots we average over power spectra produced during an interval spanning several  $t/R_*$ . On these occasions the details are given in the caption of the figure.

We show the runs with  $R_c M = 7.15$  from Table II in Fig. 10. By increasing  $N_b$  while keeping  $R_*$  the same we are able to see further into the IR for a given  $\gamma_*$ . Apart from this increasing,  $N_b$  does not have a significant effect on the shape of the power spectrum, implying that  $N_b = 8$  is sufficient to measure the slope of the power law towards the UV. Increasing  $\gamma_*$  does not change the location or amplitude of the IR peak in respect to  $R_*$ . While the slope of the power spectrum towards the IR is in agreement with  $k^{-1}$  for  $\gamma_* \simeq 2$ , it appears steeper for  $\gamma_* \simeq 4$  and  $\gamma_* \simeq 8$ . Between  $\gamma_* \simeq 4$  and  $\gamma_* \simeq 8$  the slope appears consistent.

## B. Exponential and constant nucleation

In Fig. 11, we show the evolution of the power spectra for an exponential nucleation run with  $\gamma_* \simeq 4$ . Similar to in Fig. 8 we plot the results of a simulation using the envelope approximation as detailed in [22] using the same bubble nucleation locations and times.

For the exponential nucleation run we see that the envelope simulation gives an overestimate of peak amplitude, but is still within an order of magnitude. From the full scalar field simulation we obtain a similar peak amplitude as in the simultaneous nucleation run shown in Fig. 8. This indicates that the scaling of gravitational

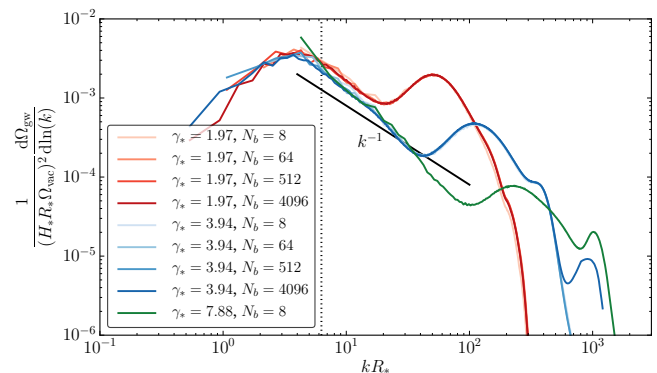


FIG. 10. Gravitational wave power spectrum for all simultaneous bubble runs with  $R_c M = 7.15$ . The parameters for these runs are given in Table II. For each simulation the power spectra have been averaged over the interval  $2.5 \leq t/R_* \leq 8.0$ . The solid black line shows a power law of  $k^{-1}$ . We plot as a vertical black dotted line the wave number  $k = 2\pi/R_*$ . See Table II for the full set of parameters of each run.

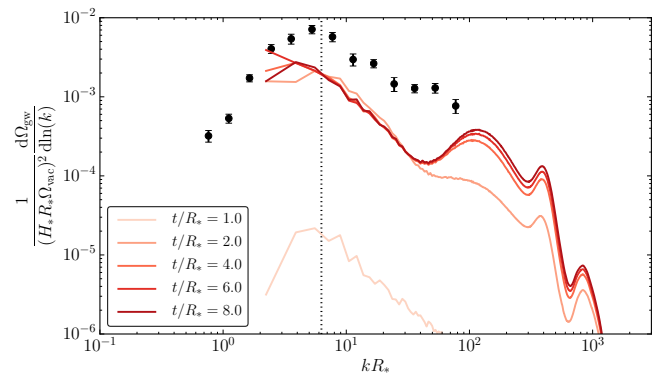


FIG. 11. Gravitational wave power spectrum for the exponential nucleation run with  $R_c M = 7.15$ ,  $N_b = 57$  and  $\gamma_* = 4.09$  listed in Table II. The vertical black dotted line marks where  $k = 2\pi/R_*$ . The black data points are the results for running a simulation with the envelope approximation with the same bubble locations and nucleation times.

wave production for our simulations is governed by  $R_*$  rather than  $\beta$ . Once again the peak location is shifted slightly into the IR in comparison to the envelope simulation.

The power spectra for all exponential simulation runs are shown in Fig. 12. For similar  $\gamma_*$ , we see convergence to the resulting slope of the power spectra for even small numbers of bubbles, implying that even  $N_b = 8$  creates a satisfactory ensemble.

All simulations seem to be consistent regarding the location and height of the peak in the IR and there is even agreement with the simultaneous nucleation runs. The slope of the power spectrum towards the IR is steeper than  $k^{-1}$  for  $\gamma_* \simeq 4$  and  $\gamma_* \simeq 8$ , and appears consistent between them.

The two constant nucleation runs listed in Table IV

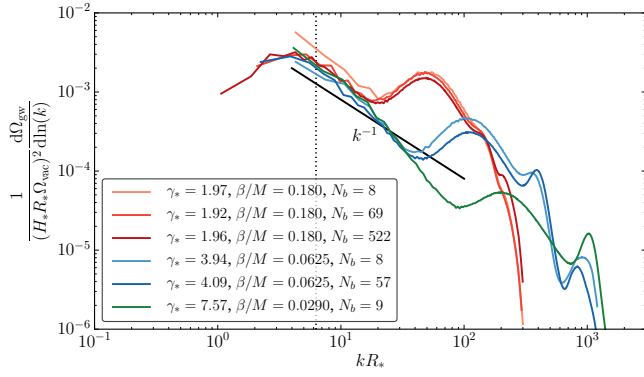


FIG. 12. Gravitational wave power spectrum for all exponential nucleation runs with  $R_c M = 7.15$ . The parameters for these runs are given in Table III. For each simulation the power spectra have been averaged over the interval  $2.5 \leq t/R_* \leq 8.0$ . The solid black line shows a power law of  $k^{-1}$ . Also plotted as a vertical black dotted line is  $kR_* = 2\pi$ .

are found to produce power spectra that are consistent with the simultaneous and exponential nucleation runs. We plot the power spectra for the constant nucleation runs along with the other  $\gamma_* \simeq 4$  runs in Fig. 15.

### C. Late time power spectrum

We are able to see the shape of the power spectrum generated during the oscillation phase by setting  $u_{ij} = 0$  after the collision phase has completed. We chose a time  $t/R_* = 2$  to set  $u_{ij} = 0$ . However for some simulations there appears to have been regions in which bubbles were still colliding at this time, and so a later time should have been chosen. For these simulations there is an uptick in the power spectrum in the IR, which can contribute significantly to the energy density. As the IR bins consist of only a few modes, there can be large oscillations in  $\Omega_{\text{gw}}$ .

The evolution of the power spectrum from the oscillation phase is shown in Fig. 13. The spectrum consists of a bump in the UV corresponding to the length scale of  $l_0$  and also a plateau extending from the bump up to just before the length scale of  $R_*$  in the IR. A similar shape can perhaps be discerned in Ref. [25], where the contribution to the total power spectrum from the oscillation phase appears to dominate. In the aforementioned study, the gravitational power spectrum from collisions was estimated to be between two and three orders of magnitude smaller than that predicted by the envelope approximation. The reason for this deficit is unclear. There was also a relatively small scale separation between  $R_*$  and  $l_0$ , as  $\gamma_*$  ranges between  $\gamma_* \simeq 2$  and  $\gamma_* \simeq 3$ . Together these may explain why the contribution from the oscillation phase dominated that of bubble collisions.

We can see that the power spectrum continues to grow during the oscillation phase. One might conclude that

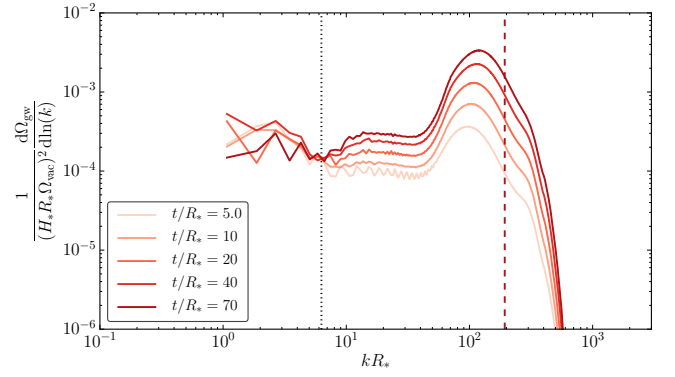


FIG. 13. Late time power spectrum from gravitational waves generated from the oscillation stage. Metric perturbations are only turned on after  $t/R_* = 2$ . This is for the run with  $R_c M = 14.3$ ,  $N_b = 512$  and  $\gamma_* = 3.94$  listed in Table V, where the full set of parameters of this run are given. The vertical black dotted line designates where  $k = 2\pi/R_*$  and the dashed red line shows where  $k = 2\pi/l_0$ .

the contribution from the oscillation phase would eventually dominate that from the bubble collisions. We therefore plot  $\Omega_{\text{gw}}$  for a set of simulations where the metric perturbations are turned on after  $t/R_* = 2.0$  in Fig. 14. We are able to estimate the growth of  $\Omega_{\text{gw}}$  during the oscillation phase from these simulations. We find that

$$\frac{d\Omega_{\text{gw}}^{\text{osc}}}{dt} \sim 10^{-1} \frac{(H_* l_0 \Omega_{\text{vac}})^2}{R_*}. \quad (47)$$

The largest amount of time that  $\Omega_{\text{gw}}^{\text{osc}}$  can grow before the growth is cut off by expansion [19] is one Hubble time  $H_*^{-1}$ .

From our earlier plots we can estimate the contribution to  $\Omega_{\text{gw}}$  from the bubble collision phase is

$$\Omega_{\text{gw}}^{\text{coll}} \sim 10^{-3} (H_* R_* \Omega_{\text{vac}})^2. \quad (48)$$

Therefore the ratio between these two contributions is

$$\frac{\Omega_{\text{gw}}^{\text{coll}}}{\Omega_{\text{gw}}^{\text{osc}}} \sim 10^{-2} (R_* H_*)^3 \frac{1}{(l_0 H_*)^2}, \quad (49)$$

$$\sim 10^{-3} \frac{H_*^3 (M_b m_{\text{Pl}})^2}{n_b \rho_c}, \quad (50)$$

where  $m_{\text{Pl}}$  is the Planck mass. For a vacuum dominated phase transition  $\rho_c \sim \rho_{\text{vac}} < \frac{1}{12\lambda} M_b^4$ .

$$\frac{\Omega_{\text{gw}}^{\text{coll}}}{\Omega_{\text{gw}}^{\text{osc}}} \gtrsim 10^{-1} \frac{H_*^3}{n_b} \left( \frac{m_{\text{Pl}}}{M_b} \right)^2. \quad (51)$$

Providing that the mass scale of the phase transition is sufficiently smaller than the Planck scale, the contribution from the collision phase should dominate.

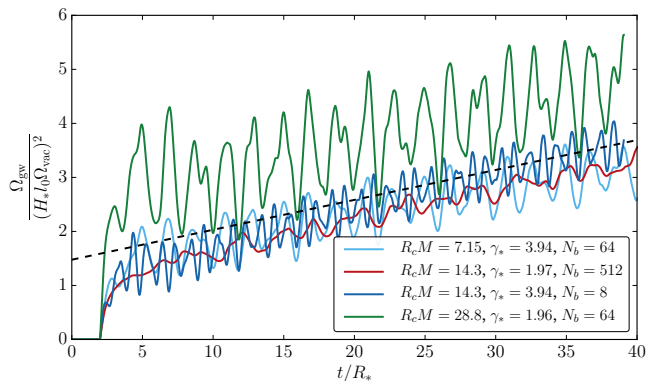


FIG. 14. Total  $\Omega_{\text{gw}}$  from gravitational waves generated after  $t/R_* = 2$  for a series of simulations with different  $R_c$ ,  $N_b$  and  $\gamma_*$ , see Table V. The oscillations are due to ringing in the IR of the power spectrum. The dashed black line is a fit for the rate of increase of  $\Omega_{\text{gw}}$ , with a slope of  $d\Omega_{\text{gw}}/dt = 0.06 (H_* l_0 \Omega_{\text{vac}})^2 / R_*$ .

#### D. Fitting

In Fig. 15, we plot gravitational wave power spectra from all simultaneous, exponential and constant nucleation runs with  $\gamma_* \simeq 4$ . We can see that they seem to be consistent, indicating that nucleation rate makes little difference to the power spectra as a function of  $kR_*$ . We can therefore provide a fit for the gravitational wave power spectrum from collisions, applying to all nucleation histories.

The first two bins of the numerical power spectra contain very few modes and are expected to be significantly affected by finite size effects. To produce our fit we shall use the largest simultaneous nucleation simulation for  $\gamma_* \simeq 4$  with  $N_b = 4096$  as this provides us with the largest dynamic range. This is the only simulation in which we can resolve the peak location after removing the first two bins.

Even so, we do not have sufficient dynamic range to be able to estimate the power law towards the IR. On causal grounds, though, it is expected that the IR power goes as  $k^3$  [37]. Our peak is somewhat broader than previously seen in the envelope approximation.

We find a fit of the following form

$$\frac{d\Omega_{\text{gw}}^{\text{fit}}}{d\ln k} = \Omega_{\text{p}}^{\text{fit}} \frac{(a+b)^c \tilde{k}^b k^a}{(b\tilde{k}^{(a+b)/c} + ak^{(a+b)/c})^c}, \quad (52)$$

where we fix  $a = 3$ . Then we find that

$$\Omega_{\text{p}}^{\text{fit}} = (3.22 \pm 0.04) \times 10^{-3} (H_* R_* \Omega_{\text{vac}})^2, \quad (53)$$

$$\tilde{k} R_* = 3.20 \pm 0.04, \quad (54)$$

$$b = 1.51 \pm 0.04, \quad c = 2.18 \pm 0.15, \quad (55)$$

with errors taken from the covariance matrix of the fit. We plot our fit in Fig. 15.

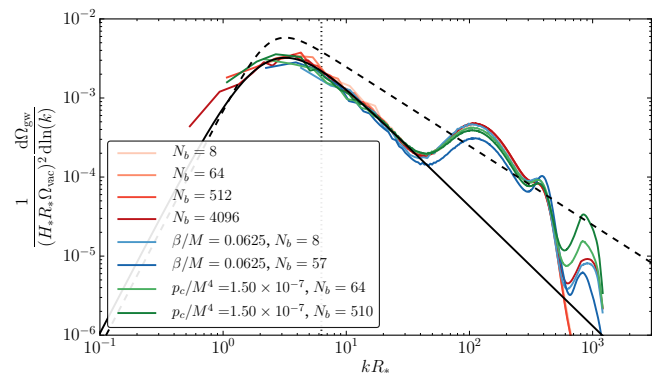


FIG. 15. Scaled gravitational wave power spectrum for all simulations with  $\gamma_* \simeq 4$ . For each simulation the power spectra have been averaged over the interval  $2.5 \leq t/R_* \leq 8.0$ . Simultaneous nucleation runs are plotted in red, exponential nucleation in blue, and constant nucleation in green. From these simulation runs we make a fit for the gravitational wave power spectrum from bubble collisions given  $R_*$ , which is shown as the black solid line. The envelope approximation fit as given in [16] is shown as the dashed black line, where we have used Eq. (56) to convert between  $\beta$  and  $R_*$ .

We provide the fit in terms of the mean bubble separation  $R_*$ , which has a clear definition in all nucleation histories, and is related to the nucleation probability through equations (21), (19) and (23), and the definition of  $R_* = n_b^{-1/3}$ . For example, for exponential nucleation,

$$\beta = \frac{(8\pi)^{1/3} v_w}{R_*}. \quad (56)$$

Using Eq. (56) with  $v_w = 0.97$  we find that

$$\frac{\Omega_{\text{p}}^{\text{fit}}}{\Omega_{\text{p}}^{\text{env}}} = 0.55, \quad (57)$$

and

$$\frac{\tilde{k}_{\text{fit}}}{\tilde{k}_{\text{env}}} = 1.0. \quad (58)$$

We plot both our fit and also the fit from the envelope approximation in Fig. 15.

## VII. CONCLUSIONS

We have performed the largest scale lattice simulations of a pure vacuum transition to date. In doing so we have been able to test the envelope approximation's description of the resulting gravitational wave power spectrum, at high bubble wall Lorentz factors  $\gamma_*$  and for many bubbles. We have simulated three different bubble nucleation histories, where bubbles are either nucleated simultaneously, with an exponentially increasing nucleation rate, or with a constant rate.

In our simulations, the peak gravitational wave power has approximate agreement with the most recent envelope approximation fit [16], to within a factor of two. The peak frequency in the envelope approximation fit has very good agreement with our results.

When the gravitational wave power is calculated using the envelope approximation's model of the actual bubbles of our simulation, the peak location is shifted towards slightly higher frequencies.

As we increase  $\gamma_*$  beyond  $\gamma_* \simeq 2$  we find that the power law on the high frequency side of the peak becomes approximately  $k^{-1.5}$ , steeper than the  $k^{-1}$  predicted by the envelope approximation.<sup>1</sup> The power law on the low frequency side is consistent with the  $k^3$  predicted by causality [37, 42], but we do not have sufficient dynamic range for an independent estimate. We provide a 3-parameter fit to our results Eq. (52).

In our simulations the overlap regions where bubbles have recently collided have extended regions in which the scalar field has large amplitude oscillations around the true vacuum, even returning to the false vacuum. These regions are not accounted for in the envelope approximation, and may be a source of its inaccuracy. Large amplitude non-linear oscillations with wavelength of order the bubble wall width  $l_0$  continue long after the bubbles finish colliding, which is also not included in the envelope approximation. These oscillations source gravitational waves which lead to an additional bump in the UV of the power spectrum at a frequency of order  $l_0^{-1}$ .

In the early Universe, the gravitational wave source will eventually diminish due to thermalisation and Hubble expansion. We find that even if the bump continues to grow for as long as a Hubble time,  $H_*^{-1}$ , the power spectrum from the oscillation phase will be subdominant

to that of bubble collisions providing that the mass of the scalar field is much less than the Planck mass.

In testing the envelope approximation and investigating the oscillatory phase of the scalar field, we have neglected the expansion of the Universe, and therefore the fit we provide strictly applies only to transitions in which the duration is much shorter than the Hubble time  $H_*^{-1}$ . There is more work to do to study the case where the Universe enters an inflationary phase before bubbles start nucleating.

## ACKNOWLEDGMENTS

We thank the Mainz Institute for Theoretical Physics (MITP) for its hospitality and support. We thank the LISA Cosmology Working Group for providing a forum to discuss our work, and extend further thanks to its coordinators Chiara Caprini and Germano Nardini. We are grateful to Stephan Huber, Ryusuke Jinno, and Kari Rummukainen for useful discussions, and to Nicola Hopkins for important contributions to this project in its early stages. Our simulations made use of the COSMOS Consortium supercomputer (within the DiRAC Facility jointly funded by STFC and the Large Facilities Capital Fund of BIS) and the Finnish Centre for Scientific Computing CSC. DC (ORCID ID 0000-0002-7395-7802) is supported by an STFC Studentship. MH (ORCID ID 0000-0002-9307-437X) acknowledges support from the Science and Technology Facilities Council (grant numbers ST/L000504/1 and ST/P000819/1). DJW (ORCID ID 0000-0001-6986-0517) was supported by Academy of Finland grant no. 286769 and the Research Funds of the University of Helsinki.

- 
- [1] B. P. Abbott et al. (Virgo, LIGO Scientific), *Phys. Rev. Lett.* **116**, 241103 (2016), arXiv:1606.04855 [gr-qc].
- [2] B. P. Abbott et al. (Virgo, LIGO Scientific), *Phys. Rev. Lett.* **116**, 061102 (2016), arXiv:1602.03837 [gr-qc].
- [3] H. Audley et al., (2017), arXiv:1702.00786 [astro-ph.IM].
- [4] C. Caprini and D. G. Figueroa, (2018), arXiv:1801.04268 [astro-ph.CO].
- [5] C. Caprini et al., *JCAP* **1604**, 001 (2016), arXiv:1512.06239 [astro-ph.CO].
- [6] D. J. Weir, in *Phil. Trans. R. Soc. A* 2018 376 20170126, Vol. A2018 (2017) p. 376, arXiv:1705.01783 [hep-ph].
- [7] S. R. Coleman, *Phys. Rev.* **D15**, 2929 (1977), [Erratum: *Phys. Rev.*D16,1248(1977)].
- [8] A. D. Linde, *Nucl. Phys.* **B216**, 421 (1983), [Erratum: *Nucl. Phys.*B223,544(1983)].
- [9] P. J. Steinhardt, *Phys.Rev.* **D25**, 2074 (1982).
- [10] E. Witten, *Phys.Rev.* **D30**, 272 (1984).
- [11] C. J. Hogan, *MNRAS* **218**, 629 (1986).
- [12] A. Kosowsky, M. S. Turner, and R. Watkins, *Phys. Rev.* **D45**, 4514 (1992).
- [13] A. Kosowsky and M. S. Turner, *Phys. Rev.* **D47**, 4372 (1993), arXiv:astro-ph/9211004 [astro-ph].
- [14] M. Kamionkowski, A. Kosowsky, and M. S. Turner, *Phys. Rev.* **D49**, 2837 (1994), arXiv:astro-ph/9310044 [astro-ph].
- [15] S. J. Huber and T. Konstandin, *JCAP* **0809**, 022 (2008), arXiv:0806.1828 [hep-ph].
- [16] T. Konstandin, (2017), arXiv:1712.06869 [astro-ph.CO].
- [17] C. Caprini, R. Durrer, and G. Servant, *Phys.Rev.* **D77**, 124015 (2008), arXiv:0711.2593 [astro-ph].
- [18] M. Hindmarsh, S. J. Huber, K. Rummukainen, and D. J. Weir, *Phys.Rev.Lett.* **112**, 041301 (2014), arXiv:1304.2433 [hep-ph].
- [19] M. Hindmarsh, S. J. Huber, K. Rummukainen, and D. J. Weir, *Phys. Rev.* **D92**, 123009 (2015), arXiv:1504.03291 [astro-ph.CO].
- [20] M. Hindmarsh, S. J. Huber, K. Rummukainen, and D. J. Weir, *Phys. Rev.* **D96**, 103520 (2017), arXiv:1704.05871

---

<sup>1</sup> This steeper power law is closer to the  $k^{-1.8}$  reported for two-bubble collisions [12, 13], widely taken to be the envelope approximation prediction before the work of Ref. [15].

- [astro-ph.CO].
- [21] M. Hindmarsh, (2016), arXiv:1608.04735 [astro-ph.CO].
- [22] D. J. Weir, Phys. Rev. **D93**, 124037 (2016), arXiv:1604.08429 [astro-ph.CO].
- [23] R. Jinno and M. Takimoto, Phys. Rev. **D95**, 024009 (2017), arXiv:1605.01403 [astro-ph.CO].
- [24] R. Jinno and M. Takimoto, (2017), arXiv:1707.03111 [hep-ph].
- [25] H. L. Child and J. T. Giblin, Jr., JCAP **1210**, 001 (2012), arXiv:1207.6408 [astro-ph.CO].
- [26] A. Kosowsky and M. S. Turner, Phys.Rev. **D47**, 4372 (1993), arXiv:astro-ph/9211004 [astro-ph].
- [27] K. Enqvist, J. Ignatius, K. Kajantie, and K. Rummukainen, Phys. Rev. D **45**, 3415 (1992).
- [28] R. Jinno, S. Lee, H. Seong, and M. Takimoto, JCAP **1711**, 050 (2017), arXiv:1708.01253 [hep-ph].
- [29] I. Garcia Garcia, S. Krippendorff, and J. March-Russell, (2016), arXiv:1607.06813 [hep-ph].
- [30] S. W. Hawking, I. G. Moss, and J. M. Stewart, Phys. Rev. D **26**, 2681 (1982).
- [31] J. Braden, J. R. Bond, and L. Mersini-Houghton, JCAP **1503**, 007 (2015), arXiv:1412.5591 [hep-th].
- [32] J. Zhang and Y.-S. Piao, Phys. Rev. **D82**, 043507 (2010), arXiv:1004.2333 [hep-th].
- [33] G. Aarts, G. F. Bonini, and C. Wetterich, Nucl. Phys. **B587**, 403 (2000), arXiv:hep-ph/0003262 [hep-ph].
- [34] R. Micha and I. I. Tkachev, Phys. Rev. Lett. **90**, 121301 (2003), arXiv:hep-ph/0210202 [hep-ph].
- [35] A. Arizabalaga, J. Smit, and A. Tranberg, Phys. Rev. **D72**, 025014 (2005), arXiv:hep-ph/0503287 [hep-ph].
- [36] J. Garcia-Bellido, D. G. Figueroa, and A. Sastre, Phys.Rev. **D77**, 043517 (2008), arXiv:0707.0839 [hep-ph].
- [37] C. Caprini, R. Durrer, T. Konstandin, and G. Servant, Phys.Rev. **D79**, 083519 (2009), arXiv:0901.1661 [astro-ph.CO].
- [38] J. F. Dufaux, A. Bergman, G. N. Felder, L. Kofman, and J.-P. Uzan, Phys. Rev. **D76**, 123517 (2007), arXiv:0707.0875 [astro-ph].
- [39] D. Daverio, M. Hindmarsh, and N. Bevis, (2015), arXiv:1508.05610 [physics.comp-ph].
- [40] J. A. Combs and S. Yip, Phys. Rev. B **28**, 6873 (1983).
- [41] M. Peyrard and M. D. Kruskal, Physica **14D**, 88 (1984).
- [42] R. Durrer and C. Caprini, JCAP **0311**, 010 (2003), arXiv:astro-ph/0305059 [astro-ph].